

Use of Plasmon Spectroscopy to Evaluate the Mechanical Properties of Materials at the Nanoscale

Vladimir P. Oleshko,* Mitsuhiro Murayama, and James M. Howe

Department of Materials Science and Engineering, University of Virginia, Charlottesville, VA 22904-4745, USA

Abstract: Relationships between volume plasmon excitations and mechanical properties of various materials are considered. Based on systematic evaluation of available data, correlations between the volume plasmon energy, E_p , Young's modulus, Y_m , bulk modulus, B_m , shear modulus, G_m , and microhardness, H_m , are established. The resulting correlations indicate that plasmon energies potentially can be used to predict and/or determine the local mechanical properties of technologically important materials, such as metal alloys, semiconductors, and ceramics at the nanometer level.

Key words: parallel electron energy-loss spectroscopy (PEELS), volume plasmons, mechanical properties, Young's modulus, bulk modulus, shear modulus, microhardness, nanostructures

INTRODUCTION

Throughout his distinguished career, Gareth Thomas has pioneered the use of advanced transmission electron microscopy (TEM) techniques to determine structure–property relationships in materials at the highest levels of resolution (refer to the many examples in Thomas, 1962, 1998; Thomas and Goringe, 1979). These efforts are particularly important now, as nanostructured materials such as quantum devices and nanocomposites have attracted considerable technological attention and are currently being manufactured. In this paper, we describe applications of plasmon spectroscopy to determine various mechanical properties of materials at the nanometer level. It is quite difficult, if not impossible, to obtain such properties for nanoscale structures, particularly metastable nanophases, by other techniques. Application of this technique may provide new

insights into understanding complex structure–property relationships in materials, which are generally determined by a number of intrinsic factors such as the atomic, crystalline, and electronic structures and bonding, and by extrinsic factors such as precipitates, impurities, grain boundaries, dislocation arrangements, and so forth. Nanoscale structures are particularly well-suited for analysis in a field-emission gun (FEG) TEM, where subnanometer electron probes can be routinely obtained and provide atomic-level spatial resolution (~ 0.1 – 0.2 nm) and an energy resolution (~ 0.7 – 1.7 eV) in parallel electron energy-loss spectra (PEELS) that are sufficient to monitor local electronic properties in a material (Egerton, 1996; Oleshko et al., 2000; Wang, 2000; Fultz and Howe, 2001). Therefore, the use of plasmon nanospectroscopy to evaluate the local mechanical properties of solid materials appears attractive.

Collective excitations of valence electrons with the creation of quantized quasi-particles (plasmons) is the primary inelastic scattering process that occurs as fast electrons pass through a thin solid specimen (Raether, 1980). Plasmon

excitations with characteristic frequencies in the low-loss region have been used to determine the dielectric function of some materials (Raether, 1980; Egerton, 1996), for compositional analysis of metal alloys (Williams and Edington, 1976), and determination of the band gap (Srivastava, 1982; Schattschneider and Jouffrey, 1995). Plasmons can exist as volume (bulk), surface, and/or interface excitations (typical frequencies $\sim 10^{16}$ Hz), making them potentially useful for diagnosing various states of matter, but practical use of plasmons in the analysis of material mechanical behavior is not widespread. It was recently realized (Gilman, 1999; Jao et al., 2001) that it might be possible to determine certain mechanical properties of materials, such as the elastic moduli or microhardness, from their volume plasmon energies. Here we present correlations between the volume plasmon energy, E_p , and Young's (elastic) modulus, Y_m , bulk modulus, B_m , shear (rigidity) modulus, G_m , and microhardness, H_m , derived for a wide variety of materials using available literature and experimental data, as well as some examples of their use to characterize local mechanical properties in materials.

EXPERIMENTAL PROCEDURES

Microstructural observations and measurements of plasmon energies in the range of 0 to 100 eV were performed on a JEOL JEM-2010F FEG TEM operating at 200 kV with a high-tilt pole piece ($C_s = 1.0$ mm and 0.23-nm point-to-point resolution) and utilizing a Gatan Imaging Filter (GIF, Model 678) with EL/P, version 3.0 and Digital Micrograph, version 2.5 software packages. The microscope allowed us to obtain PEEL spectra from precipitates and matrices either by placing a small electron probe (~ 0.5 nm in diameter) on each, or by using the 0.6-mm entrance aperture to the GIF to select each phase for analysis. Thin foils of the Ti-H (800 ppm H) and Al-Cu (4 wt.% Cu) alloys were prepared by electropolishing 3-mm disks of the heat-treated alloys with solutions of 0.5M/l $Mg(ClO_4)_2$ or 25% HNO_3 in methanol, respectively, using a twin-jet Fischione apparatus. The heat treatments and details of these samples are provided elsewhere (Tsai, 1997; Fultz and Howe, 2001). Elemental compositions of the samples were monitored using an ultrathin window LINK Pentafet energy-dispersive X-ray (EDX) detector and pulse processor interfaced with the NIST DeskTop Spectrum Analyzer software package, version 2.5.1.

RESULTS

Plasmon Energy–Mechanical Property Correlations

The linear log-log plots in Figure 1 present correlations between the average Young's moduli, Y_m , bulk moduli, B_m , and shear moduli, G_m , reported for a variety of polycrystalline materials including metals ranging in atomic number from Na to W, semiconductors, $A_{III}B_V$ compounds, carbides, hydrides, nitrides, alkali halides, and crystalline ceramics (Stephens and Brown, 1980; Hirth and Lothe, 1982; Pflugger et al., 1984; Puls, 1984; Ashby and Jones, 1986; Woo and Carpenter, 1986; Smithells, 1991; Senkov et al., 1996; Krenn et al., 1998; Callister, 2000) versus the volume plasmon energies compiled from Raether (1980), Thomas (1981), Zaluzec et al. (1981), Srivastava (1982), Ahn and Krivanek (1983), Reimer et al. (1992), Egerton (1996), and Oleshko et al. (1996), and determined experimentally. One can refer to the Appendix for individual values. Although there are sometimes variations in reported E_p values as well as in the mechanical property values for a particular material that lead to scatter in the data, it is remarkable that there is a distinct correlation between the average moduli and E_p across a wide range of materials and bonding types, with the correlation coefficient, $R = 0.88$, $SD = 0.3$ (Fig. 1a), $R = 0.80$, $SD = 0.2$ (for experimental values of B_m , Fig. 1b) and $R = 0.84$, $SD = 0.3$ (Fig. 1c). The scatter is less for any particular class of materials, such as Period 4 transition elements (Fig. 2) or covalent semiconductors (Fig. 3), even considering rather unusual low-symmetry elements such as Se and Te in Figure 3. For G_m , the elements Se and Te decrease the correlation coefficient from 0.86 to 0.80 (Fig. 3c). Figure 4 points to a linear correlation between H_m and E_p on a log-log plot for 17 primarily covalently bonded materials (As, B, C, Ge, Se, Si, Te, BN, GaSb, InSb, InAs, VN, TiN, VC, and TiC) with a little scatter ($R = 0.93$, $SD = 0.2$). In contrast to the Young's, bulk, and shear moduli, Poisson's ratio, ν , which describes the resistance of a material to transverse deformations, generally lies between 0.21 and 0.45 and varies around a mean value of 0.31 for different materials (111 data points; except Be, where $\nu = 0.02$; see the Appendix), being rather insensitive to changes of E_p . Statistical results of the linear regression analyses are summarized in Table 1.

Examples

The following experiments illustrate how the data in Figures 1–4 can be used to understand material properties at

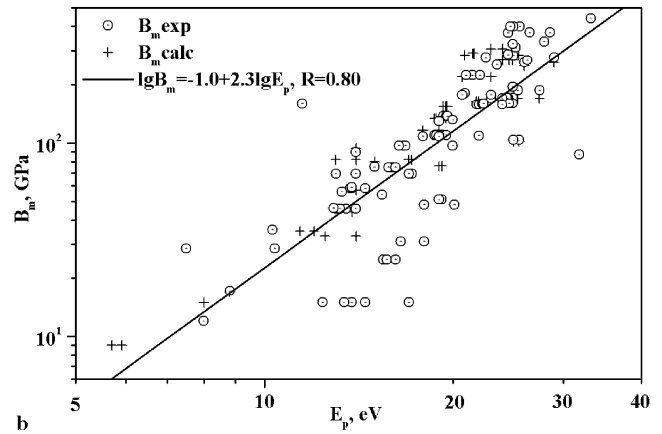
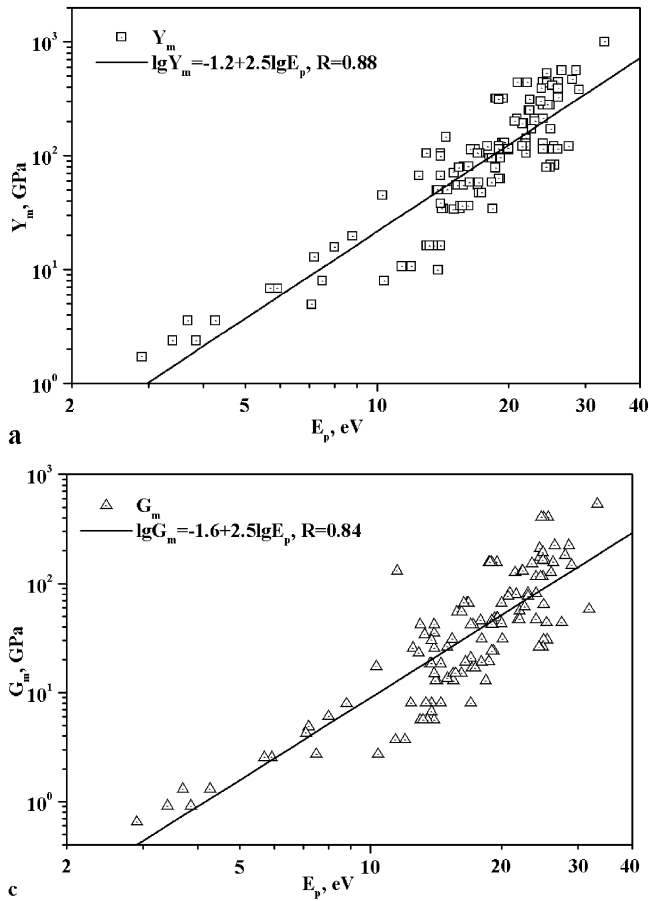


Figure 1. Volume plasmon energies, E_p , for metals, semiconductors, and ceramics versus (a) elastic modulus, Y_m ; (b) bulk modulus, B_m , \circ denotes experimental B_m values from the Appendix, $+$ denotes calculated B_m (Moruzzi et al., 1978); (c) shear modulus, G_m , plotted on a log-log scale. The solid lines represent least squares fitted linear regressions, $\lg P_m = A + B \lg E_p$, where $P_m = Y_m$ (a), B_m (b), G_m (c).

the nanometer level. They involve estimation of the elastic moduli of thin, metastable precipitates contained in the matrices of Al- and Ti-based structural materials, relative to the matrices. It is practically impossible to determine the mechanical properties of such small, metastable phases experimentally using conventional techniques.

θ' -Al₂Cu Phase in Al-Cu

A bright-field TEM image of semi-coherent, metastable θ' -Al₂Cu precipitates in an α -Al matrix taken near a $\langle 100 \rangle$ zone-axis orientation in an Al-Cu alloy is shown in Figure 5a. The θ' precipitates form as 10–20-nm-thick, disk-shaped plates several hundred nanometers in diameter on the $\{100\}$ planes in the Al-rich matrix on aging (Mondolfo, 1976). Accumulation of Cu within the θ' nanoplates was confirmed by EDX analysis using a 0.5-nm-sized electron probe. Figure 5b shows low-loss PEEL spectra obtained from the θ' -Al₂Cu precipitate (1) and the adjacent α -Al matrix (2) acquired under identical conditions. Plasmon peaks from the matrix and precipitates are readily visible

as single sharp peaks in Figure 5b. A low-intensity broadened feature at ~ 30 eV corresponds to a minor contribution of a second plasmon and could be essentially removed by a Fourier-log deconvolution (Egerton, 1996). The α -Al matrix spectrum labeled 1 has a peak value $E_p = 15.3 \pm 0.1$ eV, in agreement with typical literature values (see Appendix). The θ' plates displayed a value $E_p = 15.2 \pm 0.1$ eV. According to the data from the previous linear regression analysis (see Table 1 and Fig. 1), a plasmon peak at 15.3 eV corresponds to the following estimated values: $Y_m = 63.1$ GPa, $B_m = 50.1$ GPa, and $G_m = 25.1$ GPa. One obtains the same estimated value for the θ' precipitates because their plasmon energy is practically equal to that of α -Al. These estimates are 10.6%, 33.4%, and 4.2% less than corresponding reported average elastic moduli for polycrystalline Al at room temperature of $Y_m = 70.6$ GPa, $B_m = 75.2$ GPa, and $G_m = 26.2$ GPa, respectively (Appendix). Experimental and calculated data for the elastic moduli of the θ' phase are scarce, but values of $Y_m = 70.4$ GPa at 25°C (Bhat and Laird, 1979) and $G_m = 25.4$ GPa (Moan and Embury, 1979) have been reported.

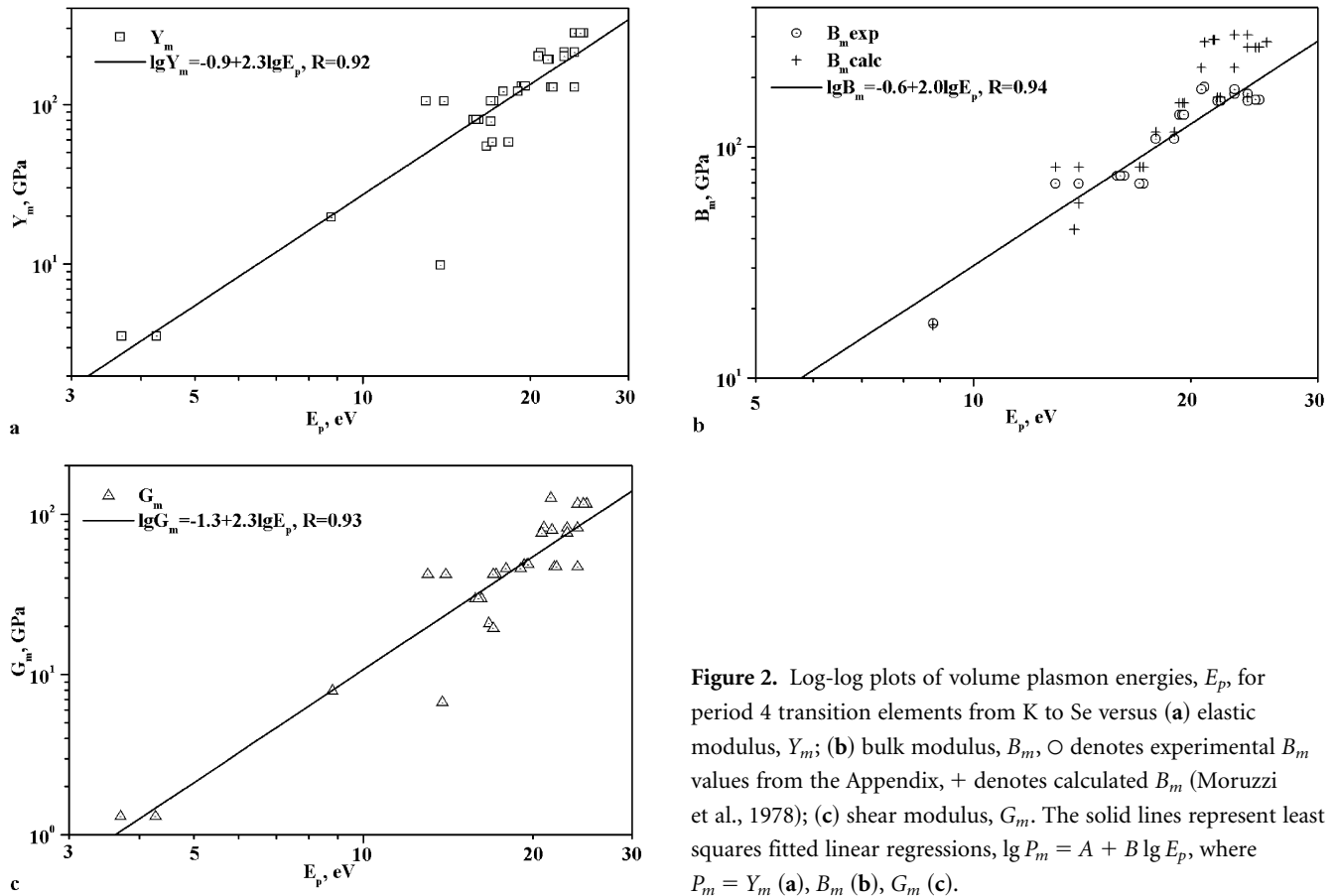


Figure 2. Log-log plots of volume plasmon energies, E_p , for period 4 transition elements from K to Se versus (a) elastic modulus, Y_m ; (b) bulk modulus, B_m , \circ denotes experimental B_m values from the Appendix, $+$ denotes calculated B_m (Moruzzi et al., 1978); (c) shear modulus, G_m . The solid lines represent least squares fitted linear regressions, $\lg P_m = A + B \lg E_p$, where $P_m = Y_m$ (a), B_m (b), G_m (c).

γ -TiH_x Phase in Ti-H Alloy

Figure 5c presents a bright-field TEM image of γ -TiH_x precipitates in an α -Ti matrix in a Ti-H alloy taken near a $\langle 01\bar{1}0 \rangle$ zone axis. Low-loss PEEL spectra acquired from TiH_x precipitates and adjacent α -Ti matrix under identical conditions are shown in Figure 5d. The PEEL spectra are dominated by bulk plasmon peaks at 17.7 ± 0.1 eV (1, matrix), at 20.1 ± 0.3 eV (2, hydride) and at 24.3 ± 0.4 eV (3, probably partially oxidized hydride phase), and also exhibit the minor Ti $M_{2,3}$ -edge starting at about 35 eV due to excitation of $3p^{1/2}$ and $3p^{3/2}$ electrons. Spectra 1 and 2 are similar to those reported by Zaluzec et al. (1981) for Ti and TiH_{1.97}, respectively, where the positions of the volume plasmon peaks were 17.2 ± 0.5 eV (17.69 eV, calculated for α -Ti) and 20.0 ± 0.5 eV (19.4 eV, calculated for TiH_{1.97}). In the case of the α -Ti matrix, our measurements are also close to the reported value of 17.9 eV (17.8 eV, calculated) by Egerton (1996) for a pure Ti film. The shift of the bulk plasmon to higher energy losses in spectrum 3 was always associated with the appearance of a second band between

11.0 and 12.8 eV, that is characteristic for titanium oxide (Ahn and Krivanek, 1983). Usually, the spectrum of this type was a minor contribution to the PEEL spectra from the α -Ti matrix and TiH_x, prevailing only occasionally. The Ti $L_{2,3}$ -edge at 455 eV and the O K-edge at about 530 eV were recorded in the inner-shell region both from the matrix and hydride phase (not shown), thus indicating the formation of partially oxidized Ti/TiH_x phases. The hydrides in Figure 5c are about 10–30 nm thick, but similar data could be obtained for smaller phases or particles, using a FEG probe or GIF entrance aperture, as mentioned previously.

According to the linear regression analyses (see Table 1 and Fig. 2), a plasmon peak at 17.7 eV corresponds to the following estimated property values: $Y_m = 100.0$ GPa, $B_m = 79.4$ GPa, and $G_m = 39.8$ GPa; this is, respectively, 16.8%, 26.8%, and 12.7% less than corresponding reported average elastic moduli for polycrystalline Ti at room temperature of $Y_m = 120.2$ GPa, $B_m = 108.4$ GPa, and $G_m = 45.6$ GPa (Appendix). A plasmon energy of 20.1 eV for the hydride phase corresponds to the estimated property values: $Y_m = 125.9$ GPa, $B_m = 100$ GPa, and $G_m = 50.1$ GPa, respectively

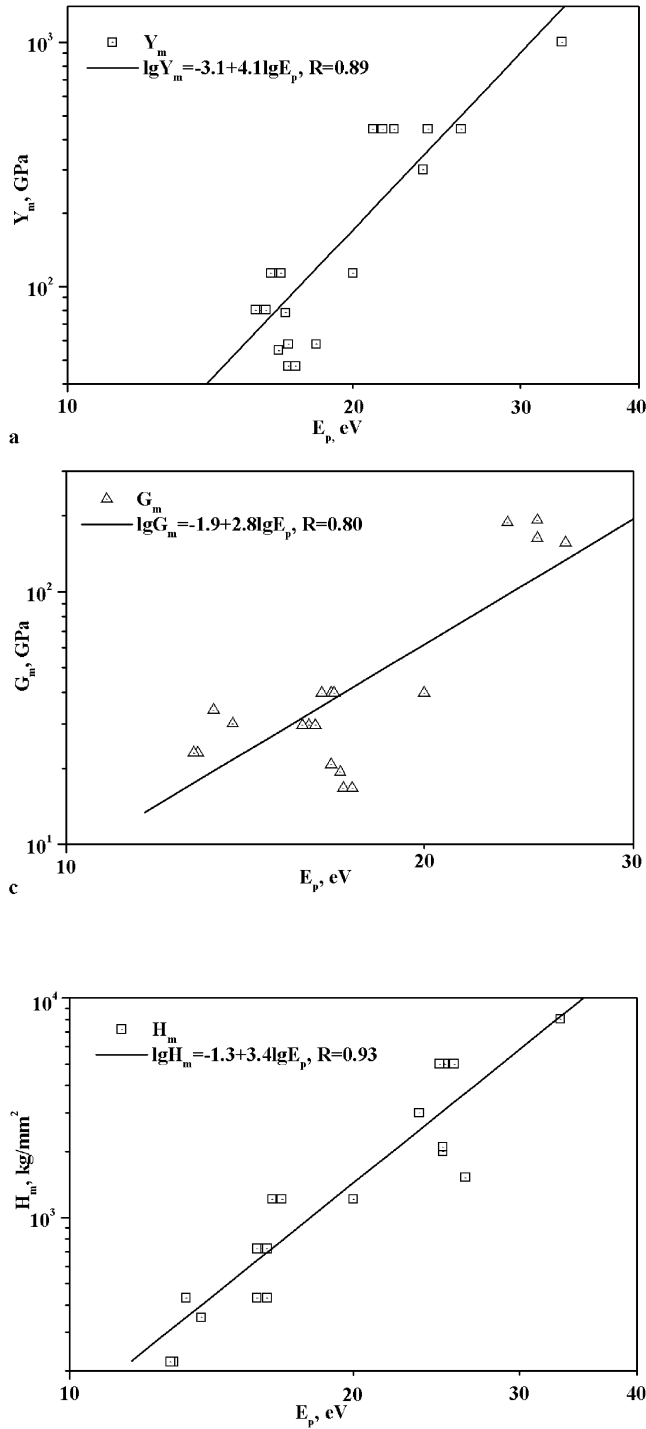


Figure 4. Log-log plot of microhardness, H_m , versus volume plasmon energy, E_p , for covalent materials shown in Figure 3. The solid line denotes a least squares fitted linear regression.

(see Table 1 and Fig. 1). For comparison, values of the elastic moduli for stoichiometric α -Ti:H = 1:2 alloy at room temperature derived from the paper by Senkov et al. (1996) are as follows: $Y_m = 114.7$ GPa, $B_m = 131.9$ GPa, and $G_m =$

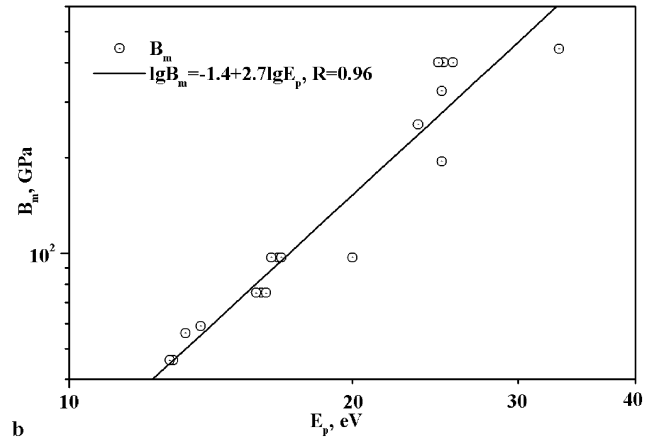


Figure 3. Log-log plots of volume plasmon energies, E_p , for covalent semiconductors (As, B, C, Ge, Se, Si, Te, GaSb, InSb, InAs, α -SiC, α -Si₃N₄, BN, VN, TiN, VC, and TiC) versus (a) elastic modulus, Y_m ; (b) bulk modulus, B_m ; (c) shear modulus, G_m . The solid lines denote least squares fitted linear regressions, $\lg P_m = A + B \lg E_p$, where $P_m = Y_m$ (a), B_m (b), G_m (c).

42.8 GPa, that is, respectively, 9.8% less for Y_m , 24.2% higher for B_m , and 17.1% less for G_m .

DISCUSSION

Plasmon Energy–Mechanical Property Correlations

The volume plasmon energy, E_p , varies with the valence electron density, n , of a material due to single-electron excitations (Raether, 1980; Egerton, 1996) approximately as:

$$E_p \cong [(\hbar\omega_p^f)^2 + E_g^2]^{0.5}, \quad (1)$$

where $\omega_p^f = [ne^2/(\epsilon_0 m)]^{0.5}$ is the free electron plasma frequency, E_g is the bandgap energy, e is the electron charge, ϵ_0 is the permittivity of vacuum, and m is the electron mass. E_p is influenced by alloy composition, bonding, and band structure. Although low-energy interband transitions can decrease the plasma frequency by increasing the effective mass of valence electrons, for all semiconductors and some

Table 1. Statistical Results of Linear Regression Analysis of log-log Correlations between Young's Modulus, Y_m , Bulk Modulus, B_m , Shear Modulus, G_m , Microhardness, H_m (Appendix), Calculated B_m (Moruzzi et al., 1978), Electron Density at the Boundary of Wigner-Seitz Cells, n_b (Alonso and March, 1989), and Volume Plasmon Energy, E_p , $\lg P = A + B \lg E_p$, $P = E_m, B_m, G_m, H_m, n_b$.

Materials	P	R	SD	N	A		B	
					Mean	SE	Mean	SE
Experimental parameters								
Metals, semiconductors (nonmetals, metalloids, A _{III} B _V), carbides, halides, hydrides, nitrides, and oxides	Y_m	0.88	0.3	136	-1.2	0.1	2.5	0.1
	B_m	0.80	0.2	110	-1.0	0.2	2.3	0.2
	G_m	0.84	0.3	131	-1.6	0.2	2.5	0.1
Transition elements of 4th period from K to Se	Y_m	0.92	0.2	37	-0.9	0.2	2.3	0.2
	B_m	0.94	0.1	28	-0.6	0.2	2.0	0.1
	G_m	0.93	0.2	35	-1.3	0.2	2.3	0.2
Covalent semiconductors (As, B, C, Ge, Se, Si, Te, GaSb, InSb, InAs, α -SiC, α -Si ₃ N ₄ , BN, VN, TiN, VC, TiC)	Y_m	0.89	0.2	23	-3.1	0.6	4.1	0.5
	B_m	0.96	0.1	23	-1.4	0.2	2.7	0.2
	G_m	0.80	0.2	24	-1.9	0.6	2.8	0.5
	H_m	0.93	0.2	26	-1.3	0.3	3.4	0.3
Calculated parameters								
Metals	B_m	0.96	0.2	56	-0.8	0.1	2.2	0.1
Metals, metalloids, and C (diamond)	n_b	0.94	0.1	129	-1.5	0.1	1.5	0.1

insulators, $E_g^2 \ll E_p^2$, so the “free-electron” approach is often a good approximation. Y_m also increases with the electron density as described by the equation for E_p above, because the bulk modulus, which is closely related to the elastic modulus, is proportional to the square root of n (Gilman, 1999). Plasmons represent longitudinal density waves (Raether, 1980), and the elastic stiffness that governs these is $B_m + 4G_m/3$. Since G_m is small for an electron liquid, B_m is the dominant term. For a variety of substances, their bulk moduli are related to plasmon energies as $B_m = \alpha E_p^2$, where α depends on the type of chemical bonding and ranges from $1-4 \times 10^{-3}$ Mbar/eV² for most materials of technological interest (Gilman, 1999). For metals bound predominantly by the outer valence s-like electrons (“simple” metals), this can be understood by applying a Wigner–Seitz model in which a metal is considered to consist of an array of positive ions immersed in an electron gas. The bulk modulus (compressibility) describes the resistance of a material to a change in volume, and, by definition, it can be expressed as:

$$B_m = -dp/(dV/V) = V(d^2U/dV^2) = (d^2U/dr^2)(dr/dV)^2, \quad (2)$$

where p is pressure, V is volume, and $U(r)$ is the internal energy expressed as a function of atomic size r , $dU/dr = 0$ and $r = r_0$ at equilibrium, $dr/dV = 1/4\pi r^2$. The analytical expression for $U(r)$ that comprises the potential energy terms related to electrostatic interaction of the electron with the positive nuclear ion, $V_a = -3e^2/2r$, and to repulsion between charged elements at different locations within the uniform negatively charged cloud, $V_r = 3e^2/5r$, and the kinetic energy, T , can be written as follows (Gilman, 1971):

$$\begin{aligned} U(r) &= V_a + V_r + T \\ &= -3e^2/2r + 3e^2/5r + 1/2m(\overline{\mathbf{p}_x^2} + \overline{\mathbf{p}_y^2} + \overline{\mathbf{p}_z^2}) \\ &= -9e^2/10r + 9h^2/32\pi^2mr^2. \end{aligned} \quad (3)$$

Here, the momentum uncertainties $\overline{\mathbf{p}_x^2} = \overline{\mathbf{p}_y^2} = \overline{\mathbf{p}_z^2} = 3h^2/16\pi^2r^2$ because of a spherical charge distribution and $\Delta x \Delta p_x = h/4\pi$ so that:

$$d^2U/dr^2 = -18e^2/10r^3 + 54h^2/32\pi^2mr^4. \quad (4)$$

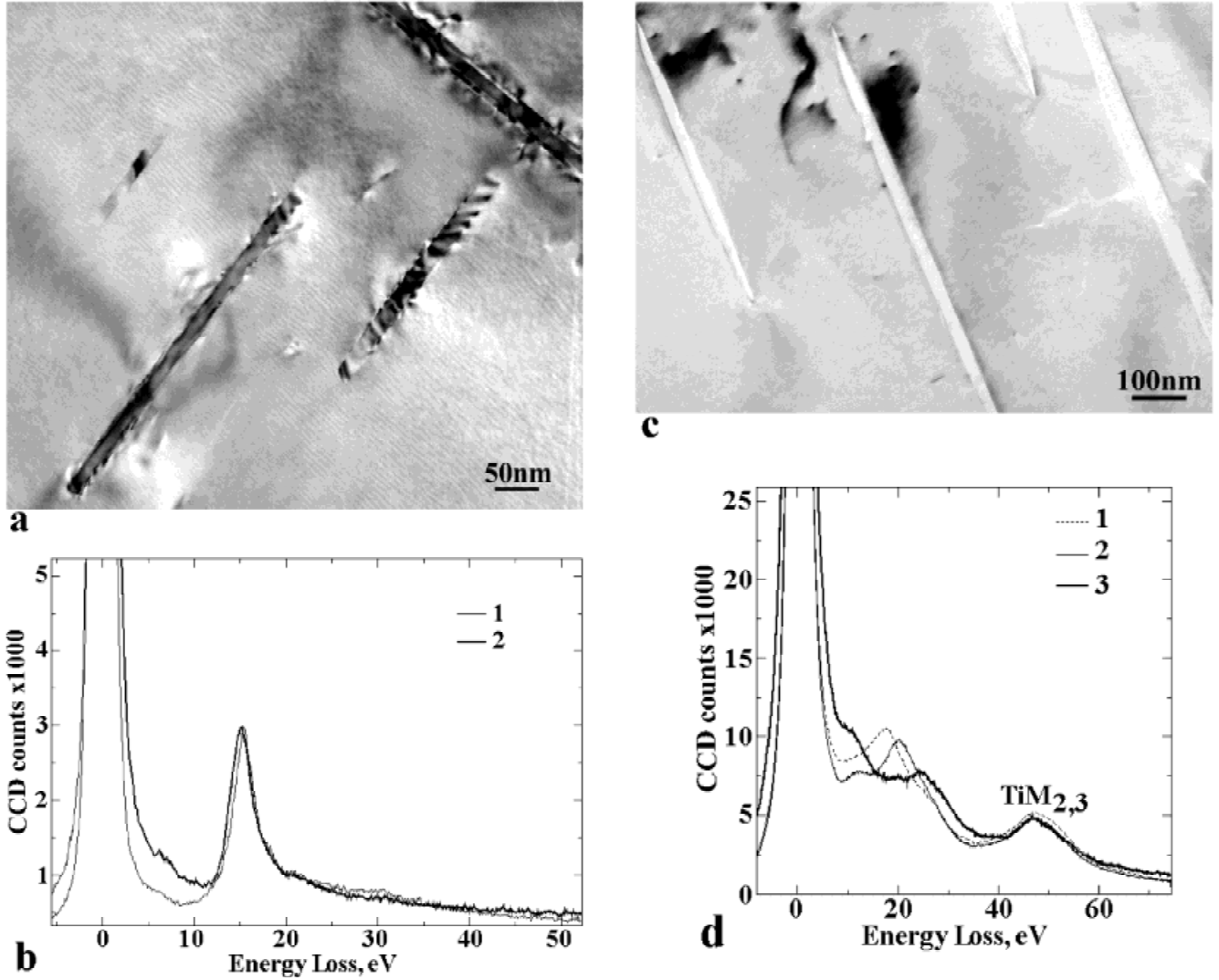


Figure 5. (a) Bright-field TEM image of θ' -Al₂Cu precipitates in an α -Al matrix in an Al-Cu alloy taken near $\langle 100 \rangle$ zone and (b) low-loss EEL spectra obtained from the θ' -Al₂Cu precipitate (1) and the adjacent α -Al matrix (2) acquired under identical conditions. (c) Bright-field TEM image of TiH_x precipitates in an α -Ti matrix in a Ti-H alloy taken near $\langle 01\bar{1}0 \rangle$ zone axis and (d) low-loss EEL spectra acquired from TiH_x precipitates (2 and 3) and the adjacent α -Ti matrix (1) under identical conditions.

At equilibrium ($dU/dr = 0$, $r = r_0$), and from equations (2) and (4):

$$\begin{aligned} d^2U/dV^2 &= (1/4\pi r^2)^2 (-18e^2/10r^3 + 54h^2/32\pi^2 m r^4) \\ &= 9e^2/160\pi^2 r_0^7, \end{aligned} \quad (5)$$

so, keeping in mind the above assumptions, for the monovalent case, one can directly relate the bulk modulus to the square of the plasmon peak energy, $E_p^2 = (h^2/4\pi^2)\omega_p^2$, as (Gilman, 1999):

$$B_m = 3e^2/40\pi r_0^4 = 8.44(me/h^2)^2 E_p^2. \quad (6)$$

Since Poisson's ratio is essentially insensitive to changes in E_p (and vice versa, see the Appendix), for isotropic matter, this leads to direct connections among the bulk, elastic, and shear moduli and the value of the volume plasmon through the relations (McClintock and Argon, 1966):

$$Y_m = 3(1 - 2\nu)B_m$$

and

$$G_m = Y_m/2(1 + \nu) = 3(1 - 2\nu)B_m/[2(1 + \nu)]. \quad (7)$$

Therefore, E_m and G_m may be expressed from equation (6), respectively, as:

$$\begin{aligned} Y_m &= 3(1 - 2\nu)B_m = 9e^2(1 - 2\nu)/40\pi r_0^4 \\ &= 16.5(1 - 2\nu) \times 10^{11}/r_0^4 \\ &= 25.32(1 - 2\nu)(me/h^2)^2 E_p^2 \end{aligned} \quad (8)$$

and

$$G_m = 12.56[(1 - 2\nu)/(1 + \nu)](me/h^2)^2 E_p^2. \quad (9)$$

These moduli are similarly related to the square of the plasmon peak energy.

The statistical results for all of the linear regression analyses shown in Figures 1–4 are summarized in Table 1. Examination of the values of B in Table 1 shows that the mean values are generally slightly higher than the ideal value of 2, that is, E_p^2 , typically ranges from 2.2 to 2.8, but compare reasonably well with the simplified model above. The greatest deviations occur for some properties associated with covalent semiconductors. In Figures 1–4, the moduli and microhardness were plotted as functions of the plasmon energy, E_p , so experimentally one can measure E_p locally in a material and use that value to estimate the corresponding mechanical properties, as illustrated by the examples in the previous results and discussed in the next section. There is significant error in making such estimates from Figures 1–4, as quantified in Table 1. For example, it may be possible to obtain only an order-of-magnitude estimate of Y_m from a value of E_p for a particular material from Figure 1a, where all material values are plotted. However, within a particular class of materials or in certain well-defined situations, this error can be significantly reduced, to within 30% of the actual values or better, as shown in Figures 2a, 3, and 4, for example.

In actuality, both the material properties and plasmon energy depend on the valence electron density. This is illustrated in Figure 6, where a log-log plot of the calculated electron density at the boundary of Wigner–Seitz cells, n_b (Alonso and March, 1989), versus E_p , for many elements—metals, metalloids (As, B, Ge, Si), and nonmetal C (diamond), 129 points in total—shows a linear regression with rather small scatter ($R = 0.94$, $SD = 0.11$). Indeed, n_b can be identified (and agrees quite well) with the interstitial electron density obtained in self-consistent Koringa–Kohn–Rostoker (KKR) local-density electron band structure

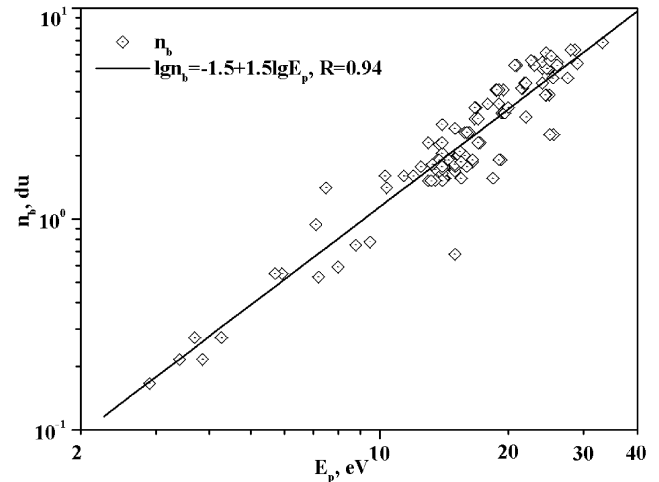


Figure 6. Log-log plot of calculated electron density at the boundary of Wigner–Seitz cells, n_b (Alonso and March, 1989), versus volume plasmon energy, E_p , for metals, nonmetals (C), and metalloids (As, B, Ge, Si), 129 points. The solid line denotes a least squares fitted linear regression.

calculations based on the muffin-tin approximation (Moruzzi et al., 1978), thus indicating that the measured volume plasmon energy is governed by the ground-state electron density, which determines the ground-state properties of a many electron assembly. Moreover, for many elements, the interstitial electron densities (Fig. 3.1 in Moruzzi et al., 1978) and experimental and calculated values of B_m and E_p (Fig. 3.4 in McClintock and Argon, 1966; Fig. 16 in Colliex, 1984) as a function of atomic number, Z , exhibit in general, similar parabolic shape behavior across each transition-metal series as a consequence of the parabolic variation of atomic volume with Z . This behavior, in particular, explains the good linear log-log correlations between E_p and calculated B_m (crosses) in Figure 1b ($R = 0.96$, $SD = 0.2$) and Figure 2b ($R = 0.94$, $SD = 0.1$).

Microhardness is not an intrinsic material property, since it represents the resistance of a material to plastic deformation and it involves the nature of dislocation motion. However, it can be related to the elastic and shear moduli through the Peierls stress (Krenn et al., 1998). Figure 4 points to a linear correlation between H_m and E_p on a log-log plot for 17 primarily covalently bonded materials (As, B, C, Ge, Se, Si, Te, GaSb, InSb, InAs, α -SiC, α -Si₃N₄, BN, VN, TiN, VC, and TiC, 26 points in total) with little scatter ($R = 0.93$, $SD = 0.2$).

The obtained correlations in many cases reflect the dominant role of the valence electron density as a basic

intrinsic factor in determining the mechanical properties of a material, although several other intrinsic factors such as the band structure (low-energy interband transitions), crystal symmetry, and type of bonding, especially, in the case compounds, may significantly influence relationships between elastic moduli and microhardness, resulting in deviations from the ideal $\lg P_m = A + 2 \lg E_p$ dependencies expected for simple metals from equations (6), (8), and (9). In macroscopic, polycrystalline materials, the observed mechanical properties may also be affected by many other extrinsic factors such as impurities, precipitates, phase morphologies, surface, defect, and interface structures (boundaries), dislocation nucleation and propagation, and so forth.

Precipitate Analyses

θ' -Al₂Cu Phase

The θ' nanoplates formed on the {100} planes (Fig. 5a) impart considerable strength to Al alloys and are often used in combination with other strengthening precipitates (Polmear, 1995). Gareth Thomas performed some of the first TEM studies on these precipitates back in 1959–1960 (Nicholson et al., 1959; Thomas and Whelan, 1959, 1960) and more recently using high-voltage TEM operating at 100, 650, and 1000 kV in the same area of a foil (Thomas, 1998). Figure 5b displays EELS data for θ' precipitate plates in the Al-Cu system (1) and the adjacent α -Al matrix (2). Although accumulation of Cu within the θ' nanoplates was confirmed by EDX analysis using a 0.5-nm-sized electron probe, the single sharp plasmon peaks from precipitates ($E_p = 15.2 \pm 0.1$ eV) and the matrix (15.3 ± 0.1 eV) almost coincide. The Appendix shows that Al has a Young's modulus $Y_m = 70.6$ GPa, bulk modulus $B_m = 75.2$ GPa, and shear modulus $G_m = 26.2$ GPa. The similar value of the plasmon energy for the θ' precipitates indicates that their elastic modulus (as well as the bulk and shear moduli) is similar to that of Al, that is, $Y_m = 70.4$ GPa (Bhat and Laird, 1979) and $G_m = 25.4$ GPa (Moan and Embury, 1979), in contrast to the case of the Ti hydrides discussed below. This further implies that the strengthening effect of θ' may arise from factors such as the ordered crystal structure and misfit of the θ' phase in the Al matrix in relation to plastic deformation, rather than to the elastic modulus of the θ' phase per se (Embury et al., 1989).

γ -TiH_x Phase

The formation of hydrides in Ti causes severe embrittlement of the alloys, making them unsuitable for applications

in H-containing environments (Senkov et al., 1996). As shown in the bright-field TEM micrograph in Figure 5c, the γ -hydride precipitates form as 25–70-nm-thick, lath-shaped particles of several hundred nanometers in length on the {01 $\bar{1}$ 0} planes in the Ti-rich matrix on aging (Bourret et al., 1986; Shih et al., 1988). *In situ* deformation TEM studies have shown that cracking occurs through the brittle hydrides and/or along the hydride/matrix interface (Shih et al., 1988). Figure 5d showed PEEL spectra obtained from the adjacent α -Ti matrix (1) and TiH_x precipitates (2, 3) acquired under identical conditions. The value of 20.1 ± 0.1 eV was found for most of the hydrides examined. This is close to the experimental value of 20.0 ± 0.5 eV and calculated value of 19.4 eV reported for TiH_{1.97} by Zaluzec et al. (1981). The Appendix shows that α -Ti has an elastic modulus $Y_m = 120.2$ GPa. Previously reported plasmon energies of 17.2 eV (Zaluzec et al., 1981), 17.9 eV (Egerton, 1996), and 19.0 eV (Reimer et al., 1992) for Ti films are similar to the experimental value of 17.7 ± 0.1 eV for the α -Ti matrix found here. According to the previous linear regression analyses (Table 1 and Fig. 2b), this corresponds to $Y_m = 100.0$ GPa (or 16.8% less than the reported value in the Appendix from Smithells, 1991), $B_m = 79.4.0$ GPa, and $G_m = 39.8$ GPa. According to Figure 1a, a plasmon peak energy $E_p = 20.1$ eV, which is approximately 3 eV higher than the surrounding matrix, indicates that the hydride particles are significantly stiffer than the α -Ti matrix. In fact, this corresponds to $Y_m = 125.9$ GPa, $B_m = 100$ GPa, and $G_m = 50.1$ GPa for the hydride phase. The higher elastic moduli as compared to the α -Ti matrix may explain the brittleness of the hydrides and the propensity for cracking through the hydrides and/or along the hydride/matrix interface.

The mechanical properties of materials depend strongly on factors such as the grain size, the sizes and morphologies of second phases, and the density of dislocations. For example, a decrease in grain size significantly increases the yield strength and hardness of metal alloys according to the Hall–Petch relationship (Hirth and Loethe, 1982). It is also known that the finite size of small particles and nanophases may confine the spatial electron distributions, thus leading to quantized energy levels (quantum size effects) and, as a result, to novel unusual mechanical, optical, and catalytic properties (Wang, 2000). However, only a limited number of theoretical studies (Fujimoto and Komaki, 1968; Ruppin and Yatom, 1976; Ruppin, 1978) and experimental data for metallic and oxidized Al (Batson et al., 1976) and Ga and Sn nanoclusters (Acheche et al., 1986) are available on the

relationship between the volume plasmon energy and peak width to particle size. These indicate that the plasmon peak energy and width should increase as the particle size decreases below about 5–10 nm, because the maximum wavelength of a volume plasmon must be equal to or smaller than the particle diameter. This change in plasmon peak energy with particle size has important consequences when applying the technique to extract information about particles or phases with dimensions less than about 10 nm, and this issue will be explored in future research.

CONCLUSIONS

The obtained correlations between the experimental and calculated average elastic moduli/microhardness and plasmon peak energy indicate that plasmon energies can be potentially used to determine the local elastic moduli and microhardness of technologically important materials. This offers a unique approach to understanding material behavior at the nanoscale, particularly when metastable phases are involved. These correlations generally reflect (but not always, especially, for compounds) the dominant influence of the valence electron density on the resulting mechanical properties. There are still questions and uncertainties associated with the technique that remain to be quantified, such as the effects of bonding and structure type on the plasmon peak energies, but the examples on the γ and θ' precipitates analyzed illustrate the potential of the technique to better understand structure–property relationships in materials.

ACKNOWLEDGMENTS

This work was supported by the Division of Materials Science and Engineering, Office of Science, U.S. Department of Energy (Grant No. DE-FG02-01ER45918). Additional support (M. M.) by the National Science Foundation (Grant No. DMR-9908855) is gratefully acknowledged.

REFERENCES

ACHECHE, M., COLLIEX, C. & TREBBIA, P. (1986). Characterization of small metallic clusters by electron energy loss spectroscopy. *Scanning Electron Micros I*, 25–32.

- AHN, C.C. & KRIVANEK, O.L. (1983). *EELS Atlas*, Warrendale, PA: Gatan.
- ALONSO, J.A. & MARCH, N.H. (1989). *Electrons in Metals and Alloys*. London, San Diego: Academic Press.
- ASHBY, M.F. & JONES, D.R.H. (1986). *Engineering Materials 1. An Introduction to Their Properties and Applications*. Oxford, U.K.: Pergamon Press.
- BATSON, P.E., CHEN, C.H. & SILCOX, J. (1976). Plasmon dispersion at large wave vectors in Al. *Phys Rev Lett* **37**, 937–940.
- BHAT, S.P. & LAIRD, C. (1979). High temperature cyclic deformation of precipitation hardened alloy, I. Partially coherent precipitates. *Acta Metal* **27**, 1861–1871.
- BOURRET, A., LASALMONTE, A. & NAKA, S. (1986). In situ high resolution observation of hydride precipitation in titanium. *Scripta Metall* **20**, 861–866.
- CALLISTER, W.D. (2000). *Materials Science and Engineering. An Introduction*, 5th ed. New York: John Wiley & Sons.
- COLLIEX, CH. (1984). Electron energy loss spectroscopy in the electron microscope. In *Advances in Optical and Electron Microscopy*, Barer, R. & Cosslett, V.E. (Eds.), p. 90. London, New York: Academic Press.
- EGERTON, R.F. (1996). *Electron Energy Loss Spectroscopy in the Electron Microscope*, 2nd ed. New York, London: Plenum Press.
- EMBURY, J.D., LLOYD, D.J. & RAMACHANDRAN, T.R. (1989). Strengthening mechanisms in aluminum alloys. In *Aluminum Alloys—Contemporary Research and Applications. Treatise on Materials Science and Technology*, Vasudevan, A.K. & Doherty, R.D. (Eds.), vol. 31, pp. 579–601. Boston, San Diego: Academic Press, Inc.
- FUJIMOTO, F. & KOMAKI, K. (1968). Plasma oscillations excited by a fast electron in a metallic particle. *J Phys Soc Japan* **25**, 1679–1687.
- FULTZ, B. & HOWE, J.M. (2001). *Transmission Electron Microscopy and Diffractometry of Materials*. Berlin: Springer-Verlag.
- GILMAN, J.J. (1971). Bulk stiffnesses of metals. *Mater Sci Eng* **7**, 357–361.
- GILMAN, J.J. (1999). Plasmons at shock fronts. *Phil Mag B* **79**, 643–654.
- HIRTH, J.P. & LOTHE, J. (1982). *Theory of Dislocations*. New York, Toronto: John Wiley & Sons.
- JAO, T.-C., LI, S., YATSUNAMI, K., CHEN, S.J., CSONTOS, A.A. & HOWE, J.M. (2001). Soot characterization and diesel engine wear. In *Proceedings of the International Tribology Conference*, vol. 3, pp. 1981–1986. Nagasaki, Japan: Japanese Society of Tribologists.
- KRENN, C.R., MORRIS, J.W. JR., JHI, S.-H. & IHM, J. (1998). Relationships between atomic bonding and intrinsic macroscopic hardness. In *Hard Coatings Based on Borides*, Kumar, A., Chung, Y.-W. & Chia, R.W.J. (Eds.), pp. 379–388. Warrendale, PA: The Minerals, Metals and Materials Society.

- McCLINTOCK, F.A. & ARGON, A.S. (1966). *Mechanical Behavior of Materials*. Reading, MA: Addison-Wesley Publishing.
- MOAN, G.D. & EMBURY, J.D. (1979). A study of Bauschinger effect in Al-Cu alloys. *Acta Metal* **27**, 903–914.
- MONDOLFO, L.F. (1976). *Aluminum Alloys: Structure and Properties*. London, Boston: Butterworths.
- MORUZZI, V.L., JANAK, J.F. & WILLIAMS, A.R. (1978). *Calculated Electronic Properties of Metals*. New York, Toronto: Pergamon Press.
- NICHOLSON, R.B., THOMAS, G. & NUTTIG, J. (1959). Electron-microscopic studies of precipitation in aluminum alloys. *J Inst Met* **87**, 429–438.
- OLESHKO, V., GIJBELS, R. & AMELINCKX, S. (2000). Electron microscopy and scanning microanalysis. In *Encyclopedia of Analytical Chemistry*, Meyers, R.A. (Ed.), pp. 9088–9120. Chichester, U.K.: Wiley & Sons, Ltd.
- OLESHKO, V., KINDRATENKO, V., GIJBELS, R., VAN ESPEN, P. & JACOB, W. (1996). Study of quasi-fractal many-particle-systems by zero-loss spectroscopic imaging, electron energy-loss spectroscopy and digital image analysis. *Mikrochimica Acta Suppl.* **13**, 443–451.
- PFLUGER, J., FINK, J., WEBER, W., BOHMEN, K.-P. & CRECELIUS, G. (1984). Dielectric properties of TiC_x , TiN_x , VC_x and VN_x from 1.5 to 40 eV determined by electron-energy-loss spectroscopy. *Phys Rev B* **30**, 1155–1162.
- POLMEAR, I.J. (1995). *Light Alloys: Metallurgy of the Light Metals*, 3rd ed. New York: Halsted Press.
- PULS, M.P. (1984). Elastic and plastic accommodation effects on metal-hydride solubility. *Acta Metall* **32**, 1259–1269.
- RAETHER, H. (1980). *Excitation of Plasmons and Interband Transitions by Electrons*, Springer Tracts in Modern Physics, vol. 88. Berlin: Springer-Verlag.
- REIMER, L., ZEPKE, U., MOESCH, J., SCHULZE-HILLERT, ST., ROSS-MESSEMER, M., PROBST, W. & WEIMER, E. (1992). *EELS Spectroscopy. A Reference Handbook of Standard Data for Identification and Interpretation of Electron Energy Loss Spectra and for Generation of Electron Spectroscopic Images*, Oberkochen, Germany: Carl Zeiss, Electron Optics Division.
- RUPPIN, R. (1978). Plasmon frequencies of small spheres. *J Phys Chem Solids* **39**, 233–237.
- RUPPIN, R. & YATOM, H. (1976). Size and shape effects on the broadening of the plasma resonance absorption in metals. *Phys Stat Sol B* **74**, 647–654.
- SCHATTSCHEIDER, P. & JOUFFREY, B. (1995). Plasmons and related excitations. In *Energy-Filtering Transmission Electron Microscopy*, Reimer L. (Ed.), pp. 151–224. Berlin: Springer-Verlag.
- SENKOV, O.N., DUBOIS, M. & JONAS, J.J. (1996). Elastic moduli of titanium-hydrogen alloys in the temperature range 20 °C to 1100 °C. *Metal Mat Trans A* **27A**, 3963–3970.
- SHIH, D.S., ROBERTSON, I.M. & BIRNBAUM, H.K. (1988). Hydrogen embrittlement of α -titanium: *In situ* TEM studies. *Acta Metall* **36**, 111–124.
- SMITHELLS, J.C. (1991). *Metals Reference Book*, 7th ed. London, Boston: Butterworths.
- SRIVASTAVA, V.K. (1982). Plasmon approach to the band gap of alkali halides. *Phys Stat Sol B* **114**, 667–671.
- STEPHENS, A.P. & BROWN, L.M. (1980). Observation by scanning transmission electron microscopy of characteristic electron energy losses due to hydrogen in transition metals. In *Electron Microscopy and Analysis 1979, Inst Phys Conf Ser*, No. 52, pp. 341–342. London and Bristol: The Institute of Physics.
- THOMAS, G. (1962). *Transmission Electron Microscopy of Metals*. New York: Wiley.
- THOMAS, G.J. (1981). Study of hydrogen and helium in metals by electron energy loss spectroscopy. In *Analytical Electron Microscopy*, Geiss R.H. (Ed.), pp. 195–197. San Francisco, CA: San Francisco Press.
- THOMAS, G. (1998). The impact of electron microscopy on materials research. Microstructural design and tailoring of advanced materials. In *Impact of Electron and Scanning Probe Microscopy on Materials Research*, Rickerby, D.G., Valdre, G. & Valdre, U. (Eds.), pp. 1–40. New York: Wiley.
- THOMAS, G. & GORINGE, M.J. (1979). *Transmission Electron Microscopy of Materials*. New York: Wiley.
- THOMAS, G. & WHELAN, M.J. (1959). Helical dislocations in quenched aluminium-4% copper alloys. *Phil Mag* **4**, 511–527.
- THOMAS, G. & WHELAN, M.J. (1960). Precipitation in Al-4%Cu alloy. In *Transformations in Metal Lattices. Proceedings of the European Regional Conference on Electron Microscopy*, vol. 1, pp. 452–455. Delft, The Netherlands.
- TSAL, M. (1997). *Determination of the Growth Mechanisms of γ -TiH in α -Ti Using High-Resolution and Energy-Filtering Transmission Electron Microscopy*. Ph.D. Thesis, University of Virginia.
- WANG, Z.L. (2000). Nanomaterials for nanoscience and nanotechnology. Transmission electron microscopy and spectroscopy of nanoparticles. In *Characterization of Nanophase Materials*, Wang, Z.L. (Ed.), pp. 1–11, 37–80. Weinheim, New York: Wiley-VCH.
- WILLIAMS, D.B. & EDINGTON, J.W. (1976). High resolution microanalysis in materials science using electron energy loss measurements. *J Microsc* **108**, 113–145.
- WOO, O.T. & CARPENTER, G.J.C. (1986). Identification of zirconium hydrides by electron energy loss spectroscopy. *Scripta Metall* **20**, 423–426.
- ZALUZEC, N.J., SCHOBER, T. & WESTLAKE, D.C. (1981). Application of EELS to the study of metal-hydrogen systems. In *Proceedings of the 39th Annual EMSA Meeting, 1981*, Bailey, G.W. (Ed.), pp. 194–195. Baton Rouge, LA: Claitor's Publishing Division.

APPENDIX

Volume plasmon energy, E_p , and average elastic modulus, Y_m , bulk modulus, B_m , shear modulus, G_m , and Poisson's ratio, ν , for various classes of materials.

Materials	Structure ^a	E_p (eV)	Ref. ^b	Y_m (GPa)	Ref. ^b	B_m (GPa)	Ref. ^b	G_m (GPa)	Ref. ^b	ν	Ref. ^b	H_m (kg/mm ²)	Ref. ^b
1	2	3	4	5	6	7	8	9	10	11	12	13	14
Elements													
Metals													
Ag thin film	FCC	25.5	R	82.7	SH	103.6	SH	30.3	SH	0.367	SH	96	KM
Ag filaments	FCC	25.5	O	82.7	SH	103.6	SH	30.3	SH	0.367	SH	96	KM
Ag thin film	FCC	25	A	82.7	SH	103.6	SH	30.3	SH	0.367	SH	96	KM
Ag polycrystalline particles	FCC	25.1	PW	82.7	SH	103.6	SH	30.3	SH	0.367	SH	96	KM
Al film	FCC	15	E	70.6	SH	75.2	SH	26.2	SH	0.345	SH	25	KM
Al thin film	FCC	15	R	70.6	SH	75.2	SH	26.2	SH	0.345	SH	25	KM
Al crystalline film	FCC	15	A	70.6	SH	75.2	SH	26.2	SH	0.345	SH	25	KM
Al crystalline film	FCC	15.3	PW	70.6	SH	75.2	SH	26.2	SH	0.345	SH	25	KM
Au thin film	FCC	24.9	E	78.5	SH	171	SH	26	SH	0.42	SH	—	—
Au thin film	FCC	24.5	R	78.5	SH	171	SH	26	SH	0.42	SH	—	—
Au thin film	FCC	24.4	A	78.5	SH	171	SH	26	SH	0.42	SH	—	—
Ba film	BCC	7.2	E	12.8	SH	—	SH	4.86	SH	0.28	SH	—	—
Be film	Hex	19.5	R	318	SH	110	SH	156	SH	0.02	SH	—	—
Be film	Hex	19	R	318	SH	110	SH	156	SH	0.02	SH	—	—
Be film	Hex	18.7	E	318	SH	110	SH	156	SH	0.02	SH	—	—
Be foil	Hex	18.8	A	318	SH	110	SH	156	SH	0.02	SH	—	—
Bi film	RHH	14.2	E	34	SH	—	—	12.8	SH	0.33	SH	—	—
Bi thin film	RHH	15.5	R	34	SH	—	—	12.8	SH	0.33	SH	—	—
Bi thin film	RHH	14.1	Ra	34	SH	—	—	12.8	SH	0.33	SH	—	—
Bi thin film	RHH	18.4	A	34	SH	—	—	12.8	SH	0.33	SH	—	—
Ca film	FCC	8.8	A	19.6	SH	17.2	SH	7.9	SH	0.31	SH	—	—
Cd film	Hex	19.2	E	62.6	SH	51	SH	24	SH	0.3	SH	—	—
Cd thin film	Hex	19	R	62.6	SH	51	SH	24	SH	0.3	SH	—	—
Ce thin film	FCC	15	R	33.5	SH	—	—	13.5	SH	0.248	SH	—	—
Co film	Hex	20.9	E	211	SH	181.5	SH	82	SH	0.32	SH	—	—
Co thin film	Hex	25.5	R	—	SH	—	—	—	SH	—	SH	—	—
Cr film	BCC	24.9	E	279	SH	160.2	SH	115.3	SH	0.21	SH	—	—
Cr thin film	BCC	24	R	279	SH	160.2	SH	115.3	SH	0.21	SH	—	—
Cr thin film	BCC	24.6	A	279	SH	160.2	SH	115.3	SH	0.21	SH	—	—
Cs film	BCC	2.9	E	1.7	SH	—	—	0.65	SH	0.295	SH	—	—
Cu film	FCC	19.3	E	129.8	SH	137.8	SH	48.3	SH	0.343	SH	76	KM
Cu thin film	FCC	19.5	R	129.8	SH	137.8	SH	48.3	SH	0.343	SH	76	KM
Cu thin film	FCC	19.6	A	129.8	SH	137.8	SH	48.3	SH	0.343	SH	76	KM
Fe film	BCC	23	E	211.4	SH	169.8	SH	81.6	SH	0.343	SH	—	—
Fe thin film	BCC	24	R	211.4	SH	169.8	SH	81.6	SH	0.343	SH	—	—
Ga film	Cub	13.8	E	9.81	SH	—	—	6.67	SH	0.47	SH	—	—
Hf film	Hex	22	R	141	SH	109	SH	56	SH	0.26	SH	—	—
In film	Tet	11.4	E	10.6	SH	—	—	3.68	SH	0.45	SH	—	—
In film	Tet	12	R	10.6	SH	—	—	3.68	SH	0.45	SH	—	—
Ir thin film	FCC	24.5	R	528	SH	371	SH	209	SH	0.26	SH	721	KM

continued

Appendix *Continued*

Materials	Structure ^a	E_p (eV)	Ref. ^b	Y_m (GPa)	Ref. ^b	B_m (GPa)	Ref. ^b	G_m (GPa)	Ref. ^b	ν	Ref. ^b	H_m (kg/mm ²)	Ref. ^b
1	2	3	4	5	6	7	8	9	10	11	12	13	14
Elements													
Metals (continued)													
K film	BCC	3.7	E	3.53	SH	—	—	1.3	SH	0.35	SH	—	—
K film	BCC	4.27	S	3.53	SH	—	—	1.3	SH	0.35	SH	—	—
La film	Hex	14	R	37.9	SH	—	—	14.9	SH	0.29	SH	—	—
Li film	BCC	7.1	S	4.91	SH	—	—	4.24	SH	0.36	SH	—	—
Li film	BCC	7.1	E	4.91	SH	—	—	4.24	SH	0.36	SH	—	—
Mg film	Hex	10.3	E	44.7	SH	35.6	SH	17.3	SH	0.291	SH	—	—
Mn film	Cub	21.6	E	191	SH	—	—	79.5	SH	0.24	SH	—	—
Mn thin film	Cub	21.5	R	191	SH	—	—	125.6	SH	0.24	SH	—	—
Mo film	BCC	26	R	324.8	SH	261.2	SH	125.6	SH	0.293	SH	—	—
Na film	BCC	5.92	E	6.8	SH	—	—	2.53	SH	0.34	SH	—	—
Na film	BCC	5.7	E	6.8	SH	—	—	2.53	SH	0.34	SH	—	—
Ni film	FCC	20.7	E	199.5	SH	177.3	SH	76	SH	0.312	SH	189	KM
Ni film	FCC	23	R	199.5	SH	177.3	SH	76	SH	0.312	SH	189	KM
Os particle	Hex	28.6	A	559	SH	373	SH	223	SH	0.25	SH	—	—
Pb film	FCC	13	E	16.1	SH	45.8	SH	5.59	SH	0.44	SH	5	—
Pb foil	FCC	14	A	16.1	SH	45.8	SH	5.59	SH	0.44	SH	5	—
Pb thin film	FCC	13.5	R	16.1	SH	45.8	SH	5.59	SH	0.44	SH	5	—
Pb film	FCC	13.2	Ra	16.1	SH	45.8	SH	5.59	SH	0.44	SH	5	KM
Pd thin film	FCC	25.4	A	121	SH	187	SH	43.6	SH	0.39	SH	—	—
Pd film	FCC	27.5	R	121	SH	187	SH	43.6	SH	0.39	SH	—	—
Pt thin film	FCC	25	R	170	SH	276	SH	60.9	SH	0.39	SH	88	KM
Pt thin film	FCC	22.6	A	170	SH	276	SH	60.9	SH	0.39	SH	88	KM
Rb film	BCC	3.41	E	2.35	SH	—	—	0.91	SH	0.3	SH	—	—
Rb film	BCC	3.86	E	2.35	SH	—	—	0.91	SH	0.3	SH	—	—
Re film	Hex	28	A	466	SH	334	SH	181	SH	0.26	SH	—	—
Rh film	FCC	29	R	379	SH	276	SH	147	SH	0.26	SH	110	KM
Ru thin film	Hex	24.5	R	432	SH	286	SH	173	SH	0.25	SH	—	—
Sb film	RHH	15.2	E	54.6	SH	—	—	—	—	—	—	—	—
Sb thin film	RHH	15.8	R	54.6	SH	—	—	—	—	—	—	—	—
Sb thin film	RHH	15.3	R	54.6	SH	—	—	—	—	—	—	—	—
Sb thin film	RHH	15.8	A	54.6	SH	—	—	—	—	—	—	—	—
Sn solid	Tet	13.7	E	49.9	SH	58.2	SH	18.4	SH	0.357	SH	—	—
Sn thin film	Tet	14.5	R	49.9	SH	58.2	SH	18.4	SH	0.357	SH	—	—
Sn thin film	Tet	13.8	A	49.9	SH	58.2	SH	18.4	SH	0.357	SH	—	—
Sr film	FCC	8	E	15.7	SH	12	SH	6.03	SH	0.28	SH	—	—
Ta film	BCC	—	A	185.7	SH	196.3	SH	69.2	SH	0.342	SH	—	—
Th particle	FCC	15.4	A	78.3	SH	54	SH	30.8	SH	0.26	SH	—	—
Ti film	Hex	17.9	E	120.2	SH	108.4	SH	45.6	SH	0.361	SH	—	—
Ti thin film	Hex	19	R	120.2	SH	108.4	SH	45.6	SH	0.361	SH	—	—
Tl film	Hex	7.5	R	7.9	SH	28.5	SH	2.71	SH	0.45	SH	—	—
Tl particle	Hex	10.4	A	7.9	SH	28.5	SH	2.71	SH	0.45	SH	—	—
V film	BCC	21.8	E	127.6	SH	158	SH	46.7	SH	0.365	SH	—	—
V thin film	BCC	22	A	127.6	SH	158	SH	46.7	SH	0.365	SH	—	—
V thin film	BCC	24	R	127.6	SH	158	SH	46.7	SH	0.365	SH	—	—

continued

Appendix Continued

Materials	Structure ^a	E_p (eV)	Ref. ^b	Y_m (GPa)	Ref. ^b	B_m (GPa)	Ref. ^b	G_m (GPa)	Ref. ^b	ν	Ref. ^b	H_m (kg/mm ²)	Ref. ^b
1	2	3	4	5	6	7	8	9	10	11	12	13	14
Elements													
Metals (Continued)													
Y film	Hex	12.5	E	66.3	SH	—	—	25.5	SH	0.265	SH	—	—
Y thin film	Hex	14	R	66.3	SH	—	—	25.5	SH	0.265	SH	—	—
Zn film	Hex	17.2	E	104.5	SH	69.4	SH	41.9	SH	0.249	SH	—	—
Zn thin film	Hex	14	A	104.5	SH	69.4	SH	41.9	SH	0.249	SH	—	—
Zn thin film	Hex	13	R	104.5	SH	69.4	SH	41.9	SH	0.249	SH	—	—
Zn thin film	Hex	17	Ra	104.5	SH	69.4	SH	41.9	SH	0.249	SH	—	—
Zr thin film	Hex	14	R	98	SH	89.8	SH	35	SH	0.38	SH	—	—
W foil	BCC	25.2	A	411	SH	311	SH	160.6	SH	0.28	SH	—	—
Nonmetals and metalloids													
As thin film	RHH	17	R	54.7	SH	—	—	20.7	SH	0.25	SH	—	—
As thin film	RHH	16.7	Ra	77.9	SH	—	—	19.3	SH	—	—	—	—
B thin film	RHH	26	R	441	AJ	—	—	—	—	—	—	—	—
B particle	RHH	24	A	441	AJ	—	—	—	—	—	—	—	—
C diamond	DC	33.2	E	1000	AJ	442	KM	534	KM	—	—	8000	KM
Ge crystalline film	DC	16.2	E	79.9	SH	75	KM	55	KM	0.32	SH	721	KM
Ge thin crystal	DC	16	R	79.9	SH	75	KM	55	KM	0.32	SH	721	KM
Ge thin crystal	DC	16	Ra	79.9	SH	75	KM	55	KM	0.32	SH	721	KM
Ge thin film	DC	16	R	79.9	SH	75	KM	55	KM	0.32	SH	721	KM
Ge thin film	DC	15.8	Ra	79.9	SH	75	KM	55	KM	0.32	SH	721	KM
Ge thin film	DC	16.2	A	79.9	SH	75	KM	55	KM	0.32	SH	721	KM
Se crystalline film	Hex	17.1	E	58	SH	—	—	—	—	0.447	SH	—	—
Se thin film	Hex	18.3	R	58	SH	—	—	—	—	0.447	SH	—	—
Si crystalline	DC	16.7	E	113	SH	97	KM	66	KM	0.42	SH	1211	KM
Si single crystal	DC	16.8	A	113	SH	97	KM	66	KM	0.42	SH	1211	KM
Si thin film	DC	20	R	113	SH	97	KM	66	KM	0.42	SH	1211	KM
Si thin film	DC	16.4	R	113	SH	97	KM	66	KM	0.42	SH	1211	KM
Te crystalline film	Hex	17.1	E	47.1	SH	—	—	16.7	SH	0.16	SH	—	—
Te particle	Hex	17.4	A	47.1	SH	—	—	16.7	SH	0.16	SH	—	—
Compounds													
A _{III} B _V													
GaAs particle	ZnS	16.2	A	—	—	—	—	—	—	—	—	430	KM
GaAs foil	ZnS	15.8	Ra	—	—	—	—	—	—	—	—	430	KM
GaSb	ZnS	13.3	A	—	—	56	KM	34-	KM	—	—	430	KM
GaSb	ZnS	13.3	Ra	—	—	56	KM	34-	KM	—	—	430	KM
InSb	ZnS	12.9	A	—	—	46	KM	23	KM	—	—	220	KM
InSb	ZnS	12.8	Ra	—	—	46	KM	23	KM	—	—	220	KM
InAs	ZnS	13.8	A	—	—	59	KM	30	KM	—	—	350	KM
InAs	ZnS	13.8	Ra	—	—	59	KM	30	KM	—	—	350	KM
Carbides													
SiC(α)	ZnS	21.5	E	440	AJ	—	—	—	—	—	—	—	—
SiC film	ZnS	21	R	440	AJ	—	—	—	—	—	—	—	—
SiC film	ZnS	22.1	Ra	440	AJ	—	—	—	—	—	—	—	—
VC	NaCl	24.9	PF	—	—	195	KM	163	KM	—	—	2094	KM
TiC	NaCl	23.5	PF	—	—	255	KM	188	KM	—	—	3000	KM

continued

Appendix Continued

Materials	Structure ^a	E_p (eV)	Ref. ^b	Y_m (GPa)	Ref. ^b	B_m (GPa)	Ref. ^b	G_m (GPa)	Ref. ^b	ν	Ref. ^b	H_m (kg/mm ²)	Ref. ^b
1	2	3	4	5	6	7	8	9	10	11	12	13	14
Compounds													
Halides													
NaCl	NaCl	15.5	E	36	HL	25	KM	15	KM	—	—	75	KM
NaCl	NaCl	16.2	Ra	36	HL	25	KM	15	KM	—	—	75	KM
NaCl particle	NaCl	16.2	A	36	HL	25	KM	15	KM	—	—	75	KM
NaCl	NaCl	15.68	S	36	HL	25	KM	15	KM	—	—	75	KM
NaF	NaCl	18	R	—	—	48	KM	31	KM	—	—	115	KM
NaF	NaCl	20.11	S	—	—	48	KM	31	KM	—	—	115	KM
LiF	NaCl	25.3	Ra	114	HL	—	—	—	—	—	—	—	—
LiF	NaCl	25.96	S	114	HL	—	—	—	—	—	—	—	—
LiF	NaCl	24	R	114	HL	—	—	—	—	—	—	—	—
LiCl	NaCl	16.5	R	—	—	31	KM	19	KM	—	—	98	KM
LiCl	NaCl	17.99	S	—	—	31	KM	19	KM	—	—	98	KM
KBr film	NaCl	14.5	R	—	—	15	KM	8	KM	—	—	58	KM
KBr film	NaCl	13.8	Ra	—	—	15	KM	8	KM	—	—	58	KM
KBr particle	NaCl	13.4	A	—	—	15	KM	8	KM	—	—	58	KM
KBr	NaCl	12.38	S	—	—	15	KM	8	KM	—	—	58	KM
Hydrides													
NbH	FCC Orth	22	SB	105	P	—	—	—	—	0.39	P	—	—
TiH _{1.5}	FCC	19	T	114	SE	130	SE	42	SE	0.33	P	—	—
TiH ₂	FCC	20	Z	115	SE	132	SE	43	SE	0.33	P	—	—
VH _{0.5}	Mon	22	Z	120	P	—	—	—	—	0.33	P	—	—
VH _{0.5}	Mon	21.5	SB	120	P	—	—	—	—	0.33	P	—	—
ZrH(γ)	FCC, Tet	19.2	WC	95	P	—	—	—	—	0.33	P	—	—
ZrH _{1.66} (δ)	FCC	18.1	Z	95	P	—	—	—	—	0.33	P	—	—
ZrH _{1.66} (δ)	FCC	18.3	WC	95	P	—	—	—	—	0.33	P	—	—
Nitrides													
BN	ZnS	25.6	Ra	—	—	400	KM	405	KM	—	—	5000	KM
BN	ZnS	25	A	—	—	400	KM	405	KM	—	—	5000	KM
BN film	ZnS	24.7	R	—	—	400	KM	405	KM	—	—	5000	KM
Si ₃ N ₄ (α)	Hex	23.7	E	300	C	—	—	—	—	—	—	—	—
TiN	NaCl	24.9	PF	—	—	325	KM	192	KM	—	—	2000	KM
VN	NaCl	26.3	PF	—	—	268	KM	156	KM	—	—	1520	KM
Oxides													
Al ₂ O ₃ (α)	RHH	26	E	390	SH	—	—	—	—	—	—	—	—
Al ₂ O ₃ thin film	RHH	23.8	A	390	SH	—	—	—	—	—	—	—	—
MgO	NaCl	22.3	E	250	AJ	160	KM	130	KM	—	—	422	KM
MgO particle	NaCl	22.4	A	250	AJ	160	KM	130	KM	—	—	422	KM
SiO ₂ (α)	Hex	22.4	E	310	AJ	—	—	—	—	—	—	—	—
SiO ₂ film	Hex	19	R	310	AJ	—	—	—	—	—	—	—	—
SrO	NaCl	31.8	A	—	—	87	KM	58	KM	—	—	167	KM
ZrO ₂	Mon	14.4	A	145	AJ	—	—	—	—	—	—	—	—

^aFCC: face centered cubic; BCC: base centered cubic; DC: diamondlike cubic; Cub: primitive cubic; Hex: hexagonal; Mon: monoclinic; Orth: orthorhombic; RHH: rhombohedral; Tet: tetragonal.

^bA: Ahn and Krivanek, 1983; AJ: Ashby and Jones, 1986; C: Callister, 2000; E: Egerton, 1996; HL: Hirth and Lothe, 1982; KM: Krenn et al., 1998; P: Puls, 1984; PF: Pflugger et al., 1984; PW: present work; O: Oleshko et al., 1996; R: Reimer et al., 1992; Ra: Raether, 1980; S: Srivastava, 1982; SB: Stephens and Brown, 1980; SE: Senkov et al., 1996; SH: Smithells, 1991; T: Thomas, 1981; WC: Woo and Carpenter, 1986; Z: Zaluzec et al., 1981.